Astron. Astrophys. 361, 5–12 (2000)

ASTRONOMY AND ASTROPHYSICS

Integral field spectroscopy of the radio galaxy 3C 171⋆

I. Márquez[1], **E. Pécontal**[2], **F. Durret**[3,4], **and P. Petitjean**[3,4]

[1] Instituto de Astrofísica de Andalucía (CSIC), Apartado 3004, 18080 Granada, Spain
[2] Observatoire de Lyon, 9 avenue Charles André, 69561 St. Genis Laval, France
[3] Institut d'Astrophysique de Paris, CNRS, 98bis Bd Arago, 75014 Paris, France
[4] DAEC, Observatoire de Paris, CNRS (UA 173), Université Paris VII, 92195 Meudon Cedex, France

Received 12 April 2000 / Accepted 29 June 2000

Abstract. We have performed integral field spectroscopy of the radio galaxy 3C 171 (redshift z=0.238) with the TIGER instrument at the Canada France Hawaii telescope in the Hβ-[OIII]4959-5007 wavelength region. We present the reconstructed Hβ and [OIII] images and compare them to the HST and radio maps. We discuss the variations of the [OIII]/Hβ line ratio throughout the nebulosity. We also analyze the velocity field in detail, in particular the presence of several components. We find that the kinematics derived with emission lines in the central region (inside 1 arcsec) are compatible with a disk-like rotation of low amplitude (50 km s^{-1}). The continuum surface brightness profile follows an $r^{1/4}$ law, suggesting that the underlying galaxy is an elliptical with an effective radius of 15 kpc.

We have fit two components in the region centered 2.7 arcsec to the West and of extension 3 arcsec^2. We find that the blueshifted component is an extension of the central part, whereas the second one is redshifted by 600 km s^{-1}. In both components, line ratios and FWHM are compatible with the presence of shocks induced by jet-cloud interactions.

Key words: galaxies: active – galaxies: individual: 3C 171 – galaxies: ISM – galaxies: kinematics and dynamics – galaxies: quasars: emission lines

1. Introduction

A number of radio galaxies and quasars at various redshifts exhibit line emission from ionized gas up to several tens or even hundreds of kiloparcsecs from the nucleus. The existence of such gaseous envelopes is most probably linked to the formation of galaxies and active nuclei. Conversely, the existence of an active nucleus influences the physical conditions of the gas, its kinematics, and star formation in the host galaxy. However, illumination of the gas by the ultraviolet radiation emitted by the active nucleus is probably not the only mechanism responsible for the ionization of the gas (Clark et al. 1998, hereafter C98, Villar-Martín et al. 1999, Tadhunter et al. 2000); the strong link between optical emission line and radio properties suggests interactions between the gas and the radio-emitting plasma, possibly because of shock heating and subsequent ionization of the gas.

Radio-loud quasars at low redshift are well adapted to the study of the interactions between the gas and radiation from the active nucleus and/or the radio plasma. This indeed becomes much more difficult for more distant objects due to their smaller spatial extent and surface brightness dimming. Integral field spectroscopy is well suited for this purpose, since, contrary to long-slit spectroscopy, it allows to fully map the velocity field in one exposure, provided the size of the ionized nebulosity is compatible with the instrument field. Such a study was done for example for three quasars with redshifts between 0.268 and 0.370 by Durret et al. (1994), for a 0.734 redshift quasar by Crawford & Vanderriest (1997), for 3C 48 by Chatzichristou et al. (1999), for four ultraluminous IRAS galaxies by Wilman et al. (1999) and for six radio-loud quasars with redshifts between 0.26 and 0.60 by Crawford & Vanderriest (2000).

3C 171 is a radio-galaxy at a redshift z=0.238 (corresponding to a scale of 3.2 kpc/arcsec for $H_0 = 75$ km s^{-1} Mpc^{-1} and q_0=0.5). It is associated with an optical emission-line region extending over 6 arcsec on either side of the nucleus (Heckman et al. 1984). These authors found large velocity gradients and striking similarities between the ionized gas and radio distributions. The radio emission itself has two bright hot spots East and West of the nucleus, and fainter emission extending perpendicularly to the radio axis, North and South of these hot spots. The correspondence between the [OIII] and radio emissions was confirmed by Baum et al. (1988) and by Blundell (1996). HST spectroscopy by Hutchings et al. (1998) has revealed outward motions of the gas at several hundred km s^{-1} in the very inner region. A line-free image of the host galaxy of 3C 171 shows a moderate elongation in the North-South direction (Baum et al. 1988). Using long slit spectra along the radio axis (PA=102) C98 have shown evidence for shocks induced by jet-cloud interactions: close radio/optical association, ionization minima almost coincident with both radio hot spots, high velocity line splitting spatially associated with the two inner hot spots, large

Send offprint requests to: isabel@iaa.es

⋆ Based on observations performed at the Canada France Hawaii Telescope

line widths in the external gas and anticorrelation between line width and ionization state in the external gas.

In this paper we present 2D spectroscopic data on 3C 171, which allow us to spatially analyse line ratios and kinematics and, used together with radio images, to interpret them in terms of an important contribution of shocks in the regions close to radio hot spots, as in the scenario reported by C98. The data are presented in Sect. 2, the morphology and excitation of the ionized gas are studied in Sect. 3, the kinematics in Sect. 4 and the discussion and conclusions in Sects. 5 and 6.

2. The data

3C 171 was observed on February 7–9, 1995 during a total exposure time of 4 hours and 13 minutes with the TIGER instrument at the 3.60m Canada France Hawaii telescope. Individual exposures were offset from one another in the East-West direction in order to cover completely the object. Airmasses were between 1.2 and 1.3. The grism used was R300, giving a spectral resolution of 6.9 Å FWHM in a spectral interval containing the HeII4686[1], Hβ and [OIII]4959–5007 lines, corresponding to a velocity resolution of 350 km s^{-1} at 6200 Å. The spatial sampling was 0.39 arcsec and each individual field about 7×7 arcsec^2; the seeing was 0.9 arcsec FWHM. The total spatial coverage is about 9×4 arcsec^2. References for a full description of the TIGER instrument and of the data reduction methods for this kind of object can be found in Durret et al. (1994).

The first steps of the data reduction (from spectra extraction to wavelength calibration) strongly depend on the instrument optics and were thus performed with the TIGER data processing software. The following stages (cosmic ray removal, photometric calibration, exposure merging, image reconstruction) were achieved using the XOasis data reduction package, dedicated to the CFHT integral field spectrograph OASIS. The algorithms of this new package are indeed more powerful than the previous ones, especially for cosmic removal and exposure merging. The reader can find a complete description of this package in the XOasis user manual at http://www-obs.univ-lyon1.fr/∼oasis/reduc/reduc_tiger_frames.html.

We also make use of the HST image (two exposures of 300s taken by the WFPC2 with the red F702W filter retrieved from the archive, realigned and summed) published by Koff et al. (1996).

We have retrieved the radio image published by Heckman et al. (1984) from the 3CRR atlas (http://www.jb.man.ac.uk). Optical and radio images have been aligned by assuming that the radio core is placed at the centroid of the brightest nuclear concentration in optical images.

3. Morphology and excitation of the ionized gas

An image and contours of the [OIII] emission reconstructed from our spectra are displayed in Fig. 1. These contours clearly reveal the inhomogeneous structure of the nebulosity, with the ionized gas extending roughly along an East-West direction up to the radio hot spots, i.e. about 5 arcsec West and 4 arcsec East of the nucleus. Strong [OIII] emission is observed in the nuclear region, as well as in two blobs on either side of the nucleus at nuclear distances of ±2.7 arcsec. The blob 2.7 arcsec West of the nucleus will hereafter be referred to as region W1.

In Fig. 1 we also show the radio emission at 1441 MHz superimposed on our [OIII] image (total emission, i.e., computed by integrating the emission in the wavelength range covered by the two [OIII] lines). It can be seen that the peaks of the radio hot spots are placed at the edges of the elongated structure in [OIII], about 2 arcsec further out than the [OIII] maxima.

A contour plot of the Hβ emission reconstructed from our spectra is displayed in Fig. 2. A region of relatively strong Hβ emission is observed almost 4 arcsec West of the nucleus, that is notably further out than region W1 observed in [OIII] West of the nucleus and therefore much closer to the radio hot spot. We will refer to it as region W2.

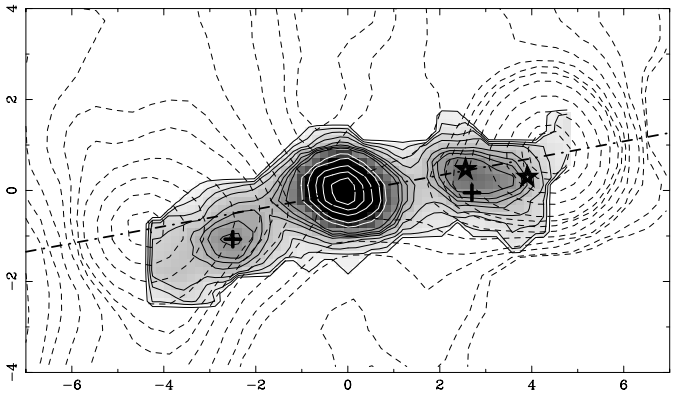

Fig. 1. Contours of the [OIII] emission reconstructed from the TIGER data, with the following values: 0.1, 0.3, 0.5, 0.7, 1, 1.2, 1.4, 1.7, 3, 4, 6, 8, and 10 (10^{-19} W m^{-2}). Radio contours are superimposed as dashed lines. The dot-dashed line joins the two radio hot spots. The positions corresponding to the spectra presented in Figs. 9 and 10 are shown with crosses. The positions of regions W1 and W2 are shown with stars. North is top and East to the left, and darker zones correspond to higher values, as in all following figures.

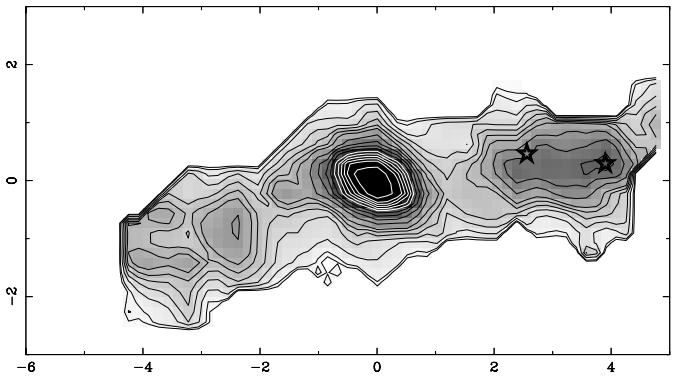

Fig. 2. Contours of the Hβ emission reconstructed from the TIGER data, with the following values: 0.03, 0.05, 0.1, 0.15, 0.2, 0.25, 0.3, 0.4, 0.5, 0.6, 0.7, 0.8, 0.9, 1, 1.1, 1.2, 1.4 (10^{-19} W m^{-2}).

[1] Note that this line is close to the filter edge and therefore the measured fluxes can be highly underestimated.

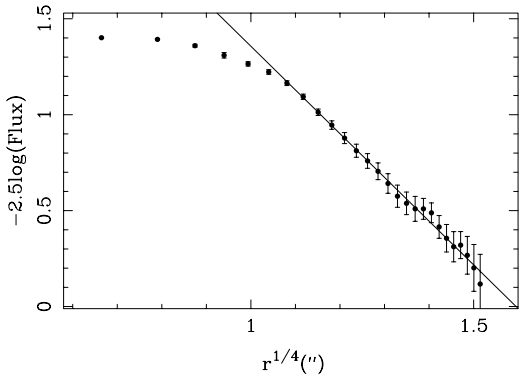

Fig. 3. Surface brightness profile obtained from the continuum image. The fit by a de Vaucouleurs law is displayed as a solid line.

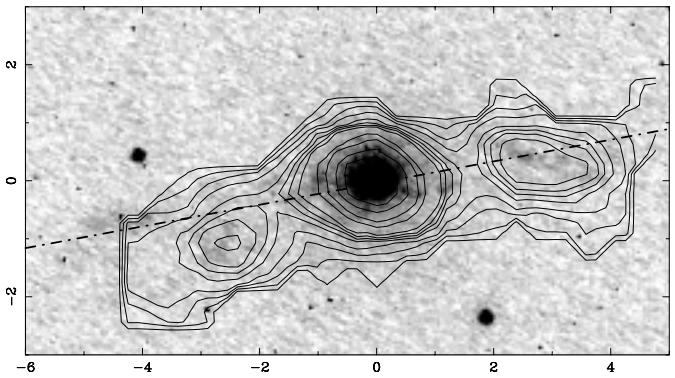

Fig. 4. [OIII] contours over HST image (filter F702W). The dot-dashed line joins the two radio hot spots.

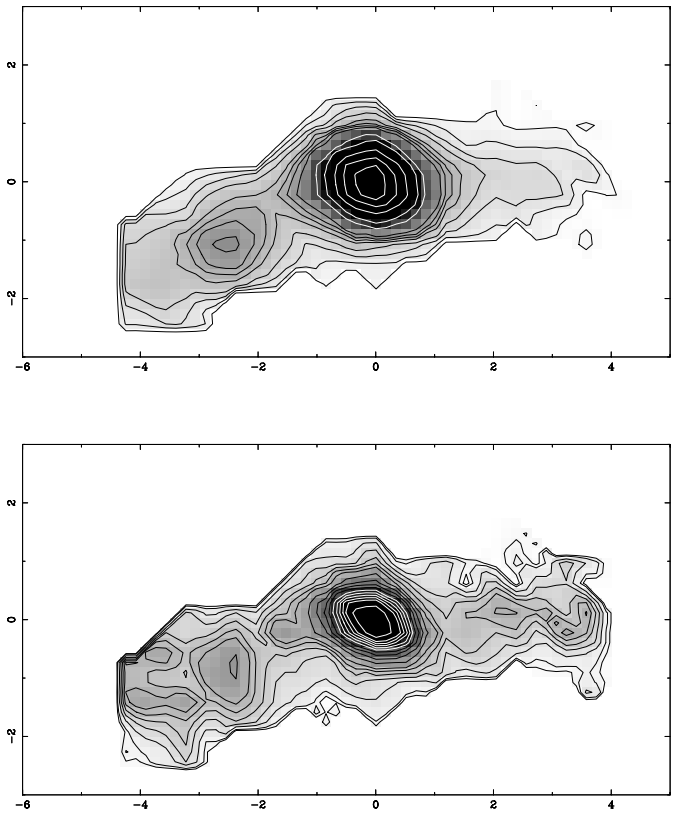

Fig. 5. Image of the blue component of [OIII] (top) and Hβ (bottom). Contour levels are 0.1, 0.3, 0.5, 0.7, 1, 1.2, 1.4, 1.7, 3, 4, 6, 8, 10 for [OIII] and 0.03, 0.05, 0.1, 0.15, 0.2, 0.25, 0.3, 0.4, 0.5, 0.6, 0.7, 0.8, 0.9, 1, 1.1, 1.2, 1.4 for Hβ (in units of 10^{-19} W m^{-2}).

We have also extracted the continuum image, reconstructed by integrating the whole wavelength range after a polynomial fit to the continuum. It only shows the central spot which is slightly resolved (FWHM $\approx$ 1.3 arcsec). We fit ellipses to the contours and obtained the resulting surface brightness profile shown in Fig. 3. A $r^{1/4}$ law fitting results in a scalelength (effective radius) of 4.8 arcsec, i. e., 15 kpc, a typical value for an elliptical galaxy.

The HST image is displayed in Fig. 4 with [OIII] contours from our image superimposed. The HST image was also convolved by the PSF estimated from our direct image to create a "smoothed HST image" which is identical to our [OIII] image, with a bright central region and two blobs coinciding with those in our [OIII] image. The similarities are easily understood by taking into account the fact that the filter used for HST observations includes the emission line contributions from [OIII] and Hα. The emission observed in the HST image is more extended to the East, with an almost linear feature well aligned with the radio axis and a brightness enhancement placed at the same position as the eastern radio hot spot. A filamentary-like feature is also observed to the West of the nucleus, corresponding to our West blob but this time not exactly aligned with the radio emission.

As shown in Sect. 4, the spectra obtained in some regions clearly indicate line splitting, with at least two components showing different excitations and kinematical behaviours: one about 3 arcsec to the West and another one 2.5 arcsec to the East. Two and three components are necessary to fit the spectra in the former and latter regions respectively; however, the signal to noise ratio (S/N) is not high enough to allow the individual fitting of each spectrum. These two regions are also marked in Fig. 1 with crosses. We have reconstructed two emission line images in order to separate each of the blue and red components of [OIII] and Hβ in the region close to W1. They are shown in Figs. 5 and 6. We stress that the peak at 2.5 arcsec to the East in Fig. 5 is located in the region where three components are present. While the morphology of the blue component is quite similar for [OIII] and Hβ, the red components are notably different, with emission peaks shifted by about 2 arcsec, corresponding to regions W1 and W2, respectively.

We have computed [OIII]/Hβ ratios for the blue and red components, rejecting the spectra where the S/N for Hβ is smaller than 1.5. The resulting images are displayed in Fig. 7. It can be noticed that, for the blue component, the regions of highest excitation are located almost symmetrically with respect to the nucleus at $\approx$ 1 arcsec in a direction almost perpendicular (PA=124) to that of the elongation of the central isophotes in Fig. 5 (PA=64). There are two local maxima, one with [OIII]/Hβ = 5 corresponding to the 3−component region, and another one with [OIII]/Hβ = 6 placed at $(-2, -1)$ arcsec. For the red component, the highest excitation is reached in the region closest to

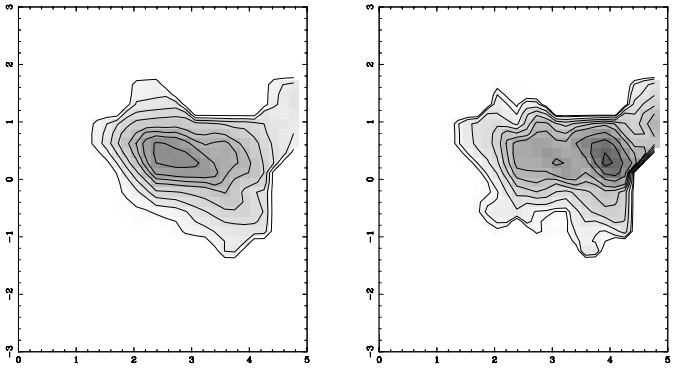

Fig. 6. Image of the red component of [OIII] (top) and Hβ (bottom). Contour levels are 0.1, 0.3, 0.5, 0.7, 1, 1.2, 1.4, 1.7, 3, 4, 6, 8, 10 for [OIII] and 0.03, 0.05, 0.1, 0.15, 0.2, 0.25, 0.3, 0.4, 0.5, 0.6, 0.7, 0.8, 0.9, 1, 1.1, 1.2, 1.4 for Hβ (in units of 10^{-19} W m^{-2}).

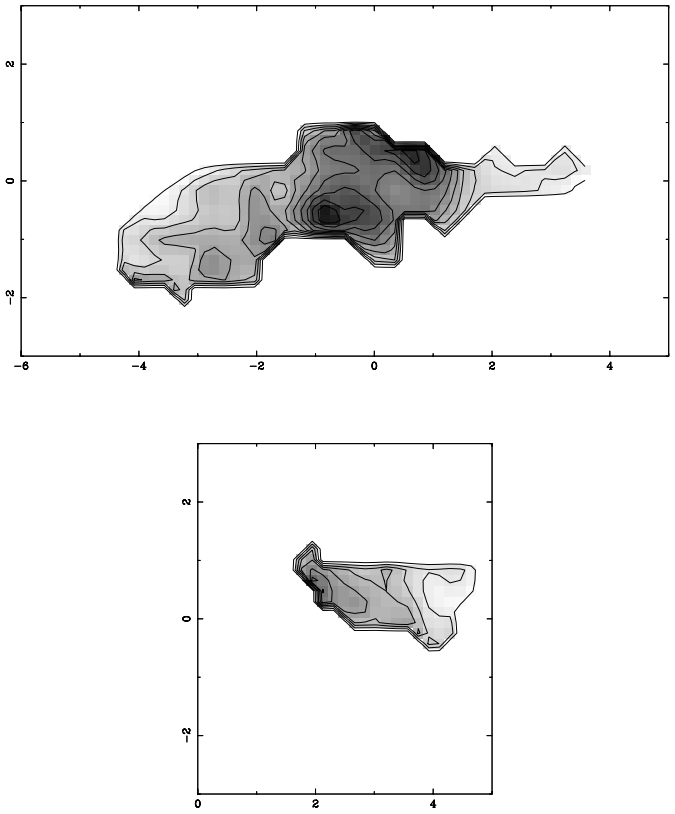

Fig. 7. [OIII]/Hβ emission line ratio for the blue (top) and the red (bottom) component. Contours range from 1 to 10 with a step of 1.

the center of the radio galaxy, with decreasing values towards the outskirts.

In order to have a high enough S/N ratio for Hβ to be able to fit [OIII] and Hβ without constraining their redshifts to be the same, we have filtered our data-cubes with a Gaussian of FWHM 1.2 arcsec. This allowed us to get more spatially extended information on [OIII]/Hβ. We then re-analysed the resulting spectra, now considering the spectra with S/N for Hβ greater than 5. The results are shown in Fig. 8. As expected, the details have been smoothed out, and now the blue component

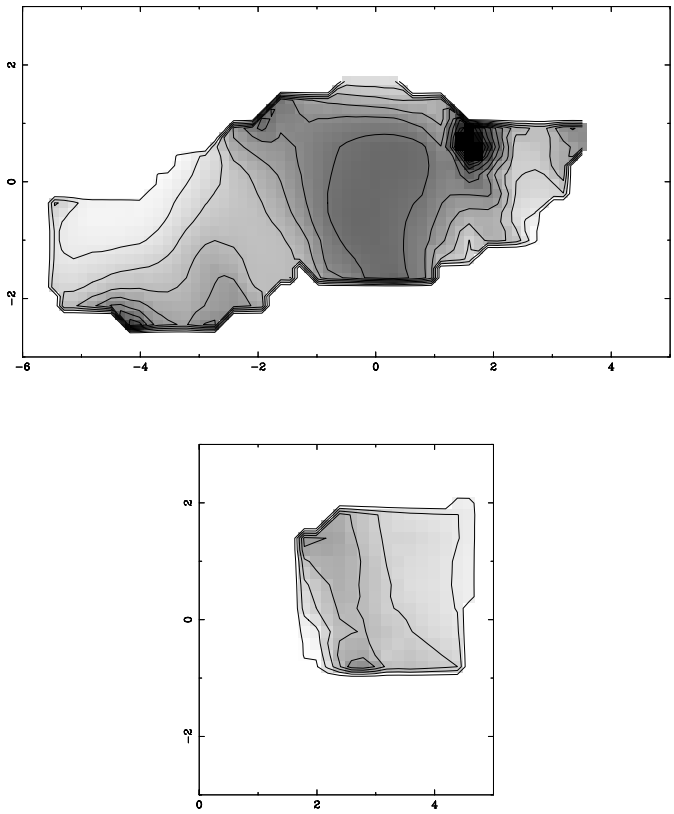

Fig. 8. [OIII]/Hβ emission line ratio for the blue (top) and the red (bottom) component (convolved, S/N>5). Contours range from 1 to 12 with a step of 1.

shows a plateau in the central region, a local peak close to the three-component region and a general trend for decreasing ratios to the East. The maximum to the West (at (1.5,1) arcsec) is due to the contribution of the red component in this region (Fig. 8, top). For the red component (Fig. 8, bottom), the behaviour is essentially the same as for the non-convolved data, but extending somewhat further.

4. Kinematics of the ionized gas

As already mentioned in Sect. 3, some of the spectra show clear signs of line splitting. These are more evident in the region about 3 arcsec to the West, where we could fit the emission lines with two components. In Fig. 9 we show the resulting fit for the region 2.7 arcsec West of the nucleus covering 3 arcsec^2. For the regions about 2.5 arcsec East of the nucleus, no fit is possible for each individual lens, but we have extracted a spectrum over about 1.4 arcsec^2 showing that at least 3 components are present (see Fig. 10). The spectrum of the nuclear region is shown in Fig. 11.

At difference with Hutchings et al. (1998) we actually detect the MgI stellar absorption line feature, from which we determine the systemic velocity to be 63126$\pm$334 km s^{-1} (the error bar is here the FWHM of the instrumental spectral line broadening, and is most probably overestimated). This value is quite close to the one derived from the [OIII] lines in the nuclear spectrum:

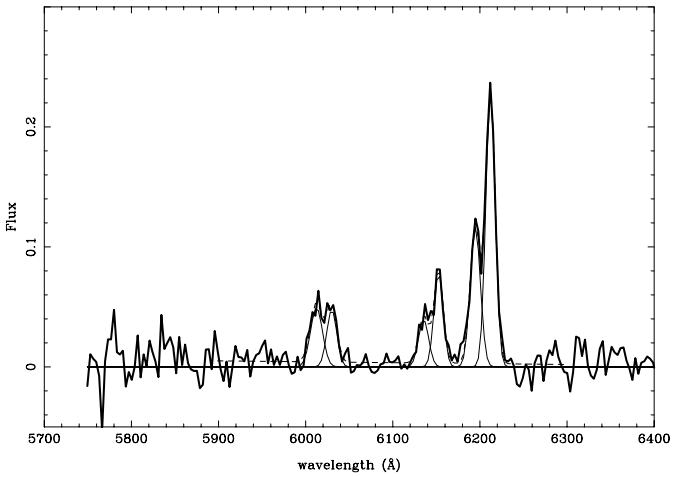

Fig. 9. Spectrum of the West region with a gaussian superimposed on each emission line.

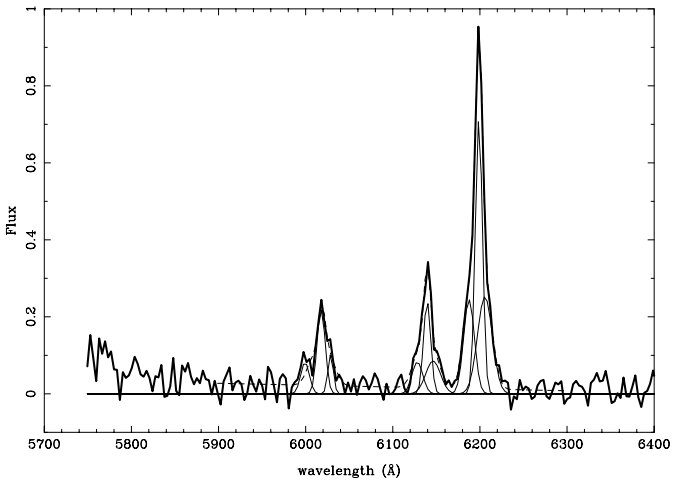

Fig. 10. Spectrum of the East region with a gaussian superimposed on each emission line.

63069 km s^{-1}. We will use this value hereafter when calculating velocities relative to the nucleus. We note that only one line of the MgI triplet is detected. This could be due to the presence of emission lines such as FeII which can be strong enough to fill the absorption lines (see e.g. Boroson & Green 1992). The low S/N (≈ 6) precludes any accurate measurement of the velocity dispersion and equivalent width of the MgI line. Note that this absorption feature is also present in the nuclear low dispersion spectra of C98 as a faint dip just left of the [NI]5199 line.

The velocity distributions have been obtained for the convolved data, for which the S/N is high enough to allow to fit [OIII] and Hβ without constraining their redshifts to be the same. Velocities and FWHM distributions for the blue and red components for the two lines are shown in Figs. 12, 13 and 14.

The kinematics of the blue component, for both Hβ and [OIII] show a central region of about 1 arcsec with rather well organized motions and almost constant FHWM $\approx$ 13–15 Å (533 to 644 km s^{-1} once corrected from instrumental broadening). They resemble typical rotation, with a kinematical position

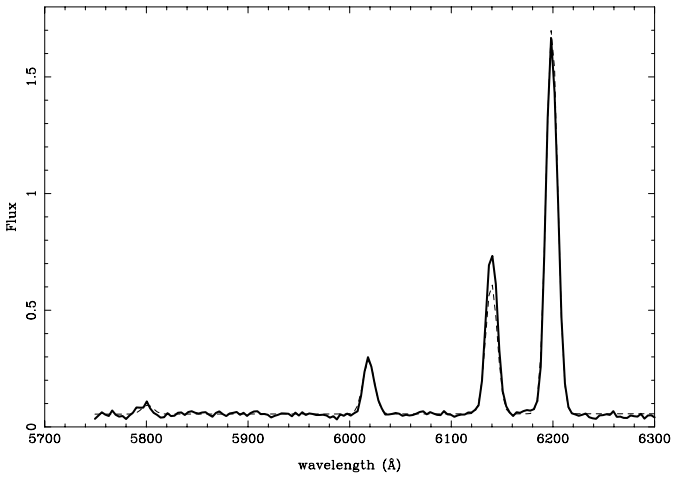

Fig. 11. Spectrum of the nuclear region with a gaussian superimposed on each emission line.

angle (PA=60) in agreement with that of the elongations seen in the corresponding emission line maps (PA=64, but see below for other possible interpretations). Kinematics are more complicated for the region to the East, with velocities positive to the North and negative to the South. We note that the FWHM reaches two local maxima of about 25 Å (1160 km s^{-1}) corresponding to the 3-component region and to the position closest to the eastern radio hot spot. From 2 arcsec outwards to the East, velocities start reaching negative values with FWHM somewhat higher that in the central region. Note that velocities and FWHM maxima are higher for Hβ than for [OIII].

The red component reaches positive velocities of about 600 km s^{-1}, but with different trends for the two lines. The peak velocity (575 km s^{-1}) and the minimum FWHM (13 Å) for Hβ coincide with W1; velocities then decrease almost along PA=0 on either side of the nucleus and FWHM reach their maxima for region W2 and to the South of W2 (18 Å, i.e., 800 km s^{-1}). [OIII] velocities are the greatest (625–600 km s^{-1}) for the central 1 arcsec of the red component, with an almost flat distribution around W1 and a sharp decrease to the South-West over W2. The FWHM of [OIII] slightly increases from East to West, with maximum values (19 Å or 856 km s^{-1}) around W2.

5. Discussion

As reported by Hutchings et al. (1998), the inner optical jet (inside $\approx$ 1 arcsec) of 3C 171 as traced by the HST image is not aligned with the radio axis. However, at larger scales the association between the optical emission lines and radio morphologies suggests that the processes producing both types of emissions are closely related. As confirmed by recent hydrodynamical simulations by Higgins et al. (1999), a collision between an extragalactic jet and a dense intergalactic cloud can lead to structures comparable to those observed in 3C171. We note that our data do not cover the tail towards the North reported by Tadhunter et al. (2000) in an Hα emission line image.

The close association between radio and emission line morphologies together with the ionization minima coincident with

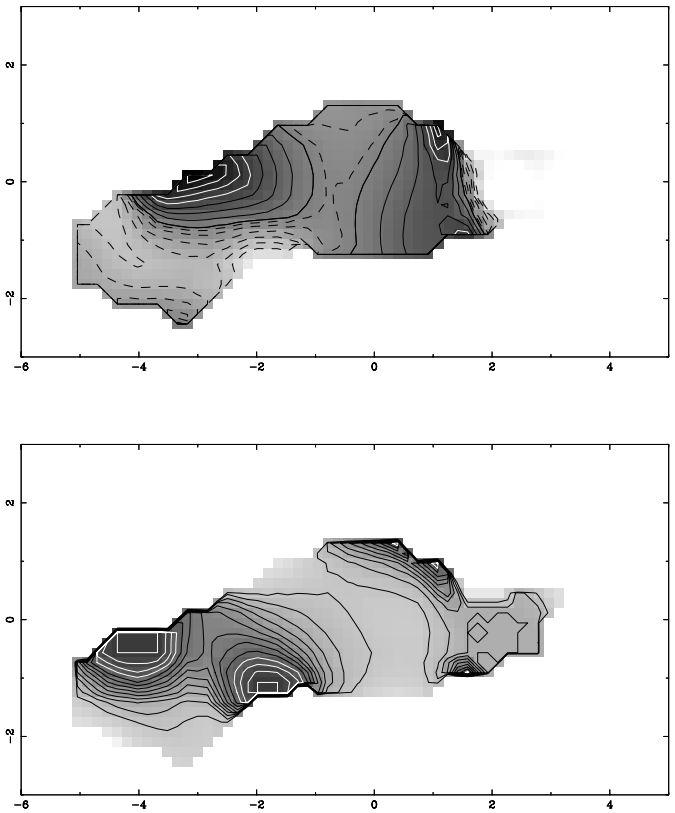

Fig. 12. Velocity (top) and FWHM (bottom) distributions of the blue component of Hβ. Velocities contours are given from -125 to 175 in steps of 25 km s^{-1}. Negative values are represented by dashed contours. FWHMs from 13 to 25 Å with step=1 Å, i.e., 533 to 1160 km s^{-1}.

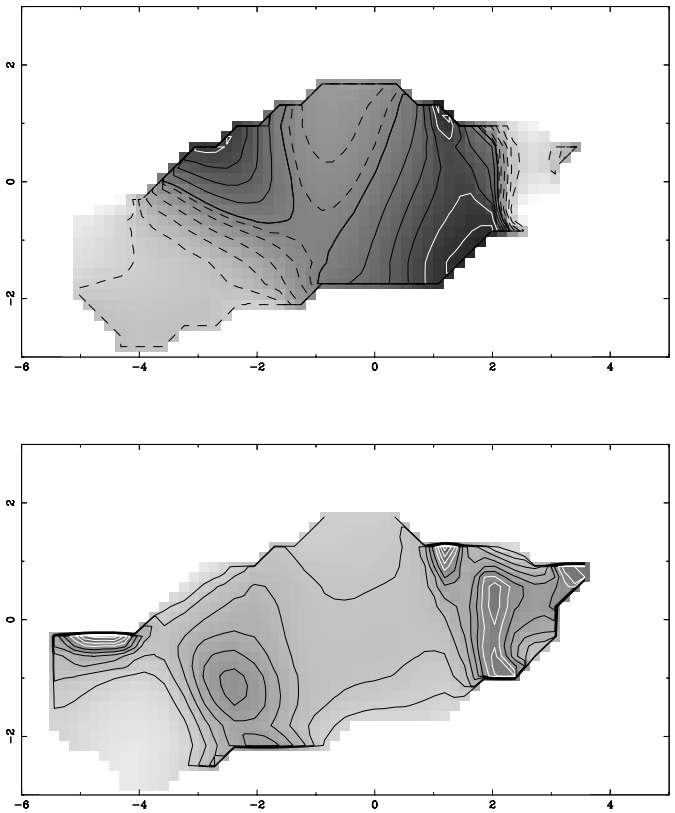

Fig. 13. Velocity (top) and FWHM (bottom) distributions of the blue component of [OIII]. Velocities contours are given from -125 to 175 in steps of 25 km s^{-1}. Negative values are represented by dashed contours. FWHMs from 13 to 21 Å with step=1 Å, i.e., 533 to 960 km s^{-1}.

both radio hot spots, the high velocity line-splitting displaced by 2 arcsec behind the hot spots, the FWHM of about 1300 km s^{-1} and the anticorrelation between line width and ionization state, have been considered as evidence for shocks induced by jet-cloud interactions (C98). C98 derive these conclusions from high (about 2 Å) and low (about 8.5 Å) resolution long slit spectra along the radio axis (PA=122), with 1.3 arcsec spatial resolution. We use 2D spectroscopic information with better spatial resolution (0.9 arcsec) but with spectral resolution of 6.9 Å. We have extracted the kinematical and emission line values for a cut along PA=122 in order to compare with their low resolution data. A general agreement is obtained. The only noticeable difference is that in our data the [OIII]/Hβ ratio reaches a local minimum at the center, followed by two maxima on either side at about 1 arcsec, probably due to a better spatial sampling (compare Figs. 7 and 8). With respect to the presence of various emission line components, we have only fit the regions where a single component fit was not satisfactory (see Sect. 4). We have only used two components for each of the [OIII] 4959, [OIII] 5007 and Hβ lines. C98 fit five components to their high resolution data, so a direct comparison is not possible.

From the two component fitting we have applied to the region to the West, we may clearly separate two regions with different kinematics and ionization states, the red one clearly detached from the blue one, which is associated with the central region. Note that the red component corresponds to the linear feature on the HST image which is not well aligned with the radio axis.

The central 2 arcsec show a velocity field that could be reminiscent of (asymmetric) rotation with an amplitude of 50 km s^{-1}. The kinematical position angle (PA=64) coincides with that of the central 1 arcsec elongated structure present in the HST image. [OIII] and Hβ trace essentially the same kinematics. Similar rotations have been found in some radio-loud quasars (Chatzichristou et al. 1999; Crawford & Vanderriest 2000). To reproduce the gas rotation we have constructed a kinematical model representing a symmetric, inclined disk rotation as a solid body out to r=1.1 arcsec and then a flat rotation curve with V$_{max}$=140 km s^{-1} (from r=1.1 to 1.4 arcsec). A non constant value of the major axis produces a better representation of the velocity field; we have fixed the kinematical major axis at PA=47° inside r=0.5 arcsec, then increasing linearly outwards to PA=67°. The adopted inclination is i=82°, derived from the ellipticity of the central body. In Fig. 15 we show the resulting isovelocity contours. In spite of the simplicity of the kinematical model, the observed velocities are reasonably well reproduced in this region. [OIII]/Hβ ratios in this central region show two maxima with [OIII]/H$\beta \approx 10$ at about 1 arcsec (3.2 kpc), at the ends of the kinematical minor axis. This result is due to the fact Hβ contours are more elongated than [OIII] contours.

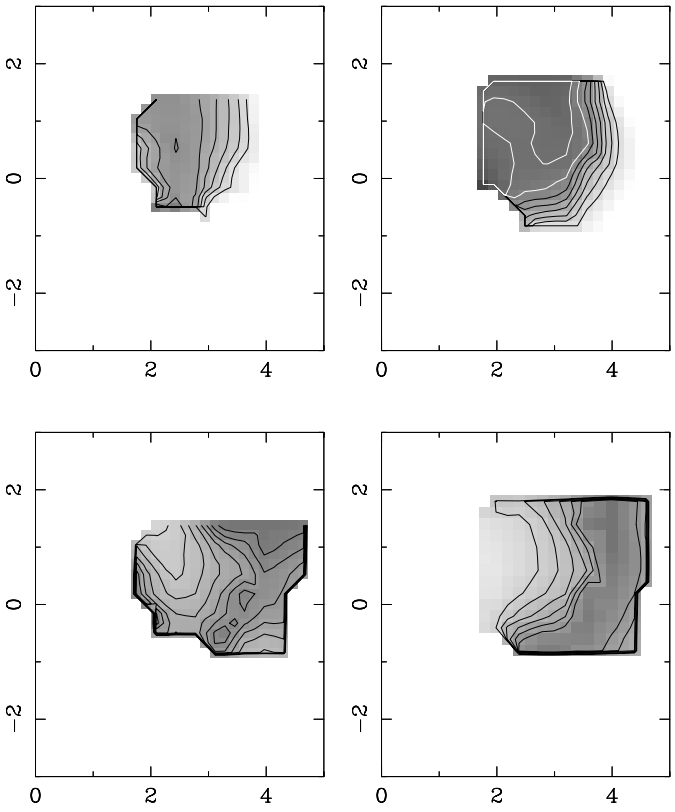

Fig. 14. Velocity (top) and FWHM (bottom) distributions of the red component of Hβ (left) and [OIII] (right). Velocities are contoured from 450 to 575 km s^{-1} (step=25 km s^{-1}) and FWHM from 11 to 17 Å (i.e., 415 to 752 km s^{-1} once corrected from instrumental broadening.)

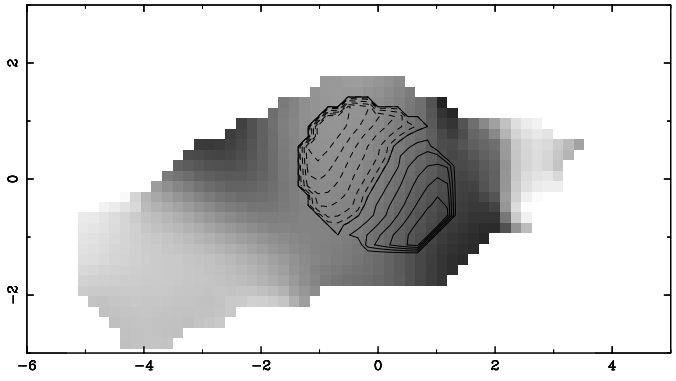

Fig. 15. Same as Fig. 13 (top) with a simple kinematic model superimposed (see text).

Based on a long slit spectrum along PA=60 with the STIS on HST, Hutchings et al. (1998) have suggested that a central outflow in this direction could also explain the observed kinematics, consistently with the clumpy emission-line structures indicating outward motions of a few $\approx$ 100 km s^{-1} within a centrally illuminated and ionized biconical region. For the sake of comparison we have extracted a cut along this PA; we obtain a small amplitude (about 80 km s^{-1}), smooth velocity distribution, where the local peaks detected by Hutchings et al. at about -0.3, 0.1 and 0.5 arcsec, are absent. Their better spatial resolution ($\approx$ 0.1 arcsec) could explain the differences. However, such a model requires a mechanism for bending the jet from PA=60 to $\sim$100 over a distance of about 1 arcsec. Notice that the spatial resolution of the radio map is not sufficient to confirm the presence of such a central jet.

The red component 3 arcsec to the West is detached by about 600 km s^{-1} from the blue one, and this cannot be reconciled with a gravitational origin. [OIII] and Hβ kinematics are slightly different, with differences up to about 200 km s^{-1} for the two lines. We note that, with the exception of the nuclear region, we do not achieve high enough S/N to extract HeII 4686 fluxes that would allow to analyze HeII/Hβ *versus* [OIII]/Hβ in the context of the models of shock + precursor of Dopita & Sutherland (1995), in the same way as Feinstein et al. (1999) for the radio galaxy 3C 299. The emission line FWHM reach values of about 860 km s^{-1} in the regions where [OIII]/Hβ ratios are minimal, in agreement with the hypothesis of jet-cloud interaction processes, as decribed by C98 (see above).

Such interactions are expected to be more important in rich environments, which seems to be the case at higher redshifts; in fact, 3C 171 has been proposed by C98 as an intermediate redshift prototype of high redshift radio galaxies. However, Baum et al. (1988) reported that 3C 171 is a very isolated object, with the closest possible companion at 200 kpc in projection. Moreover, from ROSAT X-ray images, McNamara et al. (1994) concluded that 3C 171 is not associated with a rich cluster of galaxies (whereas they did not exclude its association with a poor cluster or group). This also seems to be the case for the intermediate redshift FRII radio galaxy 3C 299; it also shows jet-cloud interaction producing shocks that ionize the gas and produce the radio optical alignement effect (Feinstein et al. 1999), and is also reported to reside in a non-cluster environment (Wan & Daly 1996; Zirbel 1997).

6. Conclusions

We have mapped for the first time the extended ionized gas around 3C 171 in the [OIII] and Hβ emission lines and derived the kinematical and physical properties. We have found that the properties of the central region can be interpreted in terms of those of a typical ENLR disk of radius 1 arcsec (3.2 kpc) following a low amplitude rotation. The continuum surface brightness profile follows an $r^{1/4}$ law, suggesting that the underlying galaxy is an elliptical with an effective radius of 15 kpc.

The kinematics are much more complicated when approaching the radio hot spots, with clear line splitting. Two components can be fit in the West region, corresponding to an extension of the central region and to a detached blob at about 600 km s^{-1}. Line ratios and FWHM are compatible with the jet-cloud interaction scenario proposed by C98.

3C 171 is quite an isolated object, at most belonging to a poor cluster or group, with properties resembling those of high redshift radio galaxies. Such high redshift radio galaxies reside in much richer environments, which are invoked to explain the origin of such jet-cloud interaction. In intermediate redshift ra-

dio galaxies showing evidence for shocks produced by jet-cloud interactions as the origin of optical-radio alignements, the mechanisms are more likely to be related with the ambient gas, since a number of these objects neither have nearby companions nor rich cluster environments.

Acknowledgements. We acknowledge discussions with E. Emsellem, P. Ferruit, J. Masegosa and M. Villar-Martín. We are also very grateful to J. Perea for his help setting up his SIPL graphics package at the IAP. This work is financed by DGICyT grants PB93-0139 and PB96-0921. Financial support to develop the present investigation has been obtained through the Junta de Andalucía.

References

Baum S.A., Heckman T., Bridle A., van Breugel W., Miley G., 1988, ApJS 68, 643
Blundell K.M., 1996, MNRAS 283, 538
Boroson T.A., Green R.F., 1992, ApJS 80, 109
Clark N.E., Axon D.J., Tadhunter C.N., Robinson A., O'Brien P., 1998, ApJ 494, 546 (C98)
Chatzichristou E.T., Vanderriest C., Jaffe E., 1999, A&A 343, 407
Crawford C.S., Vanderriest C., 1997, MNRAS 285, 580
Crawford C.S., Vanderriest C., 2000, MNRAS, astro-ph/9912306
Dopita M.A., Sutherland R.S., 1995, ApJ 455, 468
Durret F., Pécontal E., Petitjean P., Bergeron J., 1994, A&A 291, 392
Feinstein C., Macchetto F.D., Martel A.R., et al., 1999, ApJ 526, 623
Heckman T.M., van Breugel W.J.M., Miley G.K., 1984, ApJ 286, 509
Higgins S.W., O'Brien T.J., Dunlop J.S., 1999, MNRAS 309, 273
Hutchings J.B., Baum S.A., Weistrop D., et al., 1998, AJ 116, 634
Koff S., Baum S.A., Sparks W.B., et al., 1996, ApJS 107, 621
McNamara B.R., Sarazin C.L., Jannuzi B.T., 1994, BAAS 26, 1504
Tadhunter C.N., Villar-Martín M., Morganti R., Bland-Hawthorn J., Axon D., 2000, MNRAS submitted (astro-ph/0002174)
Villar-Martín M., Tadhunter C., Morganti R., Axon D., Koekemoer A., 1999, MNRAS 307, 24
Wan L., Daly R.A., 1996, ApJ 467, 145
Wilman R.J., Crawford C.S., Abraham R.G., 1999, MNRAS 309, 299
Zirbel E., 1997, ApJ 476, 489